Author: Xie, Bangwen
Title: Optical imaging of cancer and cell death
Issue Date: 2013-10-08

CHAPTER THREE

Multicolor Fluorescence Imaging of Traumatic Brain Injury in a Cryolesion Mouse Model

Based on
Smith BA*, Xie BW*, van Beek ER, Que I, Blankevoort V, Xiao S,
Cole E, Hoehn M, Kaijzel EL, Lowik CW, Smith BD. ***ACS Chem. Neurosci.***
2012 Jul 18; 3(7):530-7.

Abstract

Traumatic brain injury is characterized by initial tissue damage, which then can lead to secondary processes such as cell death and blood-brain-barrier disruption. Clinical and preclinical studies of traumatic brain injury typically employ anatomical imaging techniques and there is a need for new molecular imaging methods that provide complementary biochemical information. Here, we assess the ability of a targeted, near-infrared fluorescent probe, named PSS-794, to detect cell death in a brain cryolesion mouse model that replicates certain features of traumatic brain injury. In short, the model involves brief contact of a cold rod to the head of a living, anesthetized mouse. Using noninvasive whole-body fluorescence imaging, PSS-794 permitted visualization of the cryolesion in the living animal. *Ex vivo* imaging and histological analysis confirmed PSS-794 localization to site of brain cell death. The nontargeted, deep-red Tracer-653 was validated as a tracer dye for monitoring blood-brain-barrier disruption, and a binary mixture of PSS-794 and Tracer-653 was employed for multicolor imaging of cell death and blood-brain-barrier permeability in a single animal. The imaging data indicates that at 3 days after brain cryoinjury the amount of cell death had decreased significantly, but the integrity of the blood-brain-barrier was still impaired; at 7 days, the blood-brain-barrier was still three times more permeable than before cryoinjury.

Keywords

Traumatic brain injury, multicolor fluorescence imaging, cell death imaging, blood-brain-barrier, annexin V, zinc(II)-dipicolylamine

Introduction

Traumatic brain injury (TBI) is a major public health concern in the United States with 1.7 million people sustaining a TBI annually [1]. Over 2 % of the US population is believed to experience TBI-associated disabilities, accounting for approximately $60 billion annually in direct and indirect costs [2]. TBI is a highly heterogeneous disorder that can manifest different pathophysiological changes depending on the type, severity, and location of the brain injury. TBI is typically characterized in two stages: 1) the primary injury at the site of impact which results in tissue damage and hemorrhaging, and 2) the delayed secondary insult that represents non- mechanical damage due to continuous pathological processes. These pathological processes include blood-brain barrier disruption, edema, oxidative stress, inflammation and cell death [3]. Clinical presentation of the secondary insult is usually delayed and believed to be sensitive to therapeutic intervention. Thus, the secondary pathological processes may be viable options as therapeutic and imaging targets for treatment and diagnosis of TBI.

In the clinic, computed tomography and magnetic resonance imaging are routinely used for brain imaging of TBI [4,5]. Both modalities rely on morphological changes which occur later in the disease process; thus, TBI diagnosis and prognosis would be better served using molecular imaging techniques that target early-stage biochemical changes [6]. Fluorescence optical imaging is an attractive option for preclinical research due to its inherent safety and high sensitivity, but very few optical imaging probes have been evaluated in animal models of TBI [7]. There is a specific need for deep-red and near-infrared fluorescent probes that allow relatively deep penetration of the light through skin and tissue. An attractive concept is the possibility of multicolor imaging using multiple probes in a single animal; each probe with its distinctive wavelength and ability to report on different biomolecular processes. At present, there is a small but growing number of literature examples of simultaneous multicolor *in vivo* optical imaging [8,9,10]. In the case of TBI, imaging studies would be greatly facilitated by the development of protocols that employ a mixture of a targeted probe for cell death and a non-targeted tracer for blood-brain-barrier (BBB) permeability. This requires two sets of technical advances: 1) development and validation of deep-red and near-infrared fluorescent imaging and tracer probes that enable multicolor *in vivo* imaging in living animals, and 2) straightforward pre-clinical TBI models that are amenable to optical imaging. Here we address both needs by adapting a preclinical mouse model for TBI and investigating a set of complementary fluorescent imaging probes.

Numerous fluorescent imaging probes have been developed to specifically target biomarkers associated with cell death, but the most popular biomarker for *in vivo* imaging is phosphatidylserine exposure on the plasma membrane [11,12,13]. Imaging results with protein-based probes are promising, but technical problems such as the poor pharmacokinetics have combined to limit translation into the clinic [14,15,16,17]. It is quite challenging to alter the pharmacokinetics of proteins, so there is motivation to develop cell death imaging probes with low molecular weight [18,19,20]. We have contributed to this research topic by designing synthetic fluorescent zinc(II)-dipicolylamine probes that can distinguish the anionic membranes of dead and dying cells over the near neutral membranes of healthy cells [21]. To facilitate *in vivo* imaging, we developed PSS-794, a zinc(II)-dipicolylamine probe containing a near-infrared carbocyanine fluorophore. PSS-794 can identify cell death in a number of animal models [22,23,24]. In this current study, we demonstrate the ability of PSS-794 to non-invasively detect cell death in a brain cryolesion TBI mouse model using whole-body, epi-fluorescence imaging. Specifically, we compare cell death imaging performance of PSS-794 and fluorescently labeled Annexin V, a well-known protein-based probe for cell death imaging [25]. We also describe the non-targeted, deep-red dye, Tracer-653, for monitoring blood-brain-barrier disruption, and a binary mixture of PSS-794 and Tracer-653 for multicolor imaging of cell death and blood-brain-barrier permeability in a single animal.

Results

The study examined four fluorescent imaging probes (Fig. 1). Two of the probes, the synthetic zinc(II)-dipicolylamine complex, PSS-794, and the dye-labeled protein, Annexin-Vivo 750, are known to selectively target the anionic membranes of dead and dying cells via bridging cations (zinc and calcium respectively). It is worth noting that PSS-794 is formulated as a zinc complex primarily to improve water solubility. Although the zinc complex is labile, the bloodstream concentration of Zn^{2+} (10-20 µM) is high enough to not limit the three component assembly of apo-PSS-794, Zn^{2+}, and phosphatidylserine at the membrane surface [26]. The other two probes, Tracer-794 and Tracer-653, are non-targeted fluorophores that diffuse through the blood pool, and thus serve to measure permeability of the BBB [27,28]. Tracer-794 has the same near-infrared fluorophore as PSS-794 and so is an excellent control compound to evaluate the effect of the attached zinc(II)-dipicolylamine targeting unit. Tracer-653 is a bright and stable deep-red dye that does not self-aggregate or associate with serum proteins. Furthermore, it has a narrow emission band that can be monitored simultaneously with near-infrared PSS-794 in the same animal using different imaging filter sets (filter sets for PSS-794 ex: 705-780 nm, em: 810- 885 nm; filter sets for Tracer-653 ex: 615-665 nm, em: 695-770 nm). The specific targeting of the four fluorescent probes was tested in an adapted brain cryolesion mouse model that induces rapid breakdown of the BBB causing vasogenic brain edema and tissue damage [29]. In short, two separate cohorts of athymic mice (n = 5) were anesthetized by isoflurane inhalation. A metal cylinder with a 3 mm diameter was pre-cooled in liquid nitrogen and applied to each mouse's head for 60 s. Individual mice then received an intracardiac injection of either PSS-794 (3.0 mg/kg), Tracer-794 (3.0 mg/kg), or Annexin-Vivo 750 and imaged in an IVIS Spectrum at 3 h, 6 h and 24 h post-probe injection. Figure 2 shows representative images at the different timepoints. Immediately after probe injection, there is apparent accumulation of Tracer-794 at the site of cryolesion but the tracer soon clears from the animal. At 3 h post-probe injection, cell death probes PSS-794 and Annexin-Vivo 750 both produce high contrast signals at the site of cryoinjury. In the case of PSS-794, the image intensity at the site of cryoinjury is higher at the 3 h time point compared to the 0 h time point, indicating a relatively slow rate of probe accumulation on the surface of the dead and dying cells. As expected, the Annexin-Vivo 750 also showed extensive accumulation in the kidneys [16,30]. Target to non-target (T/NT) quantification of *in vivo* images was performed by region of interest (ROI) analysis that compared the mean pixel intensities (MPI) at the cryoinjury site (T) to MPI at a non-target site (NT) on the lower back (Fig. 3). PSS-794 exhibited the highest T/NT at the 3 h timepoint (6.77 ± 0.47; T/NT ± SEM; P < 0.003), and then decreased. In contrast, the T/NT for Annexin-Vivo 750 increased incrementally to a value of 4.87 ± 0.54 at the 24 h endpoint, reflecting a slower rate of clearance from the non-target site.

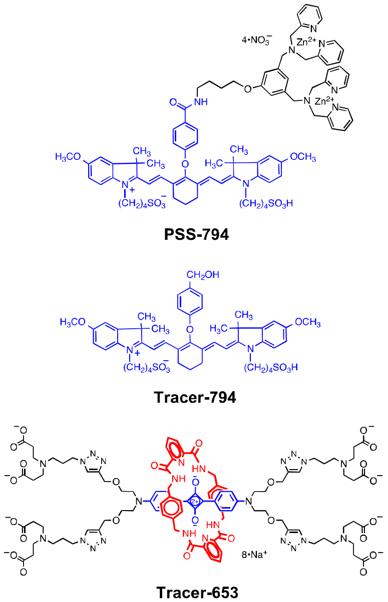

PSS-794

Tracer-794

Tracer-653

Figure 1. Chemical structures of PSS-794, Tracer-794, and Tracer-653.

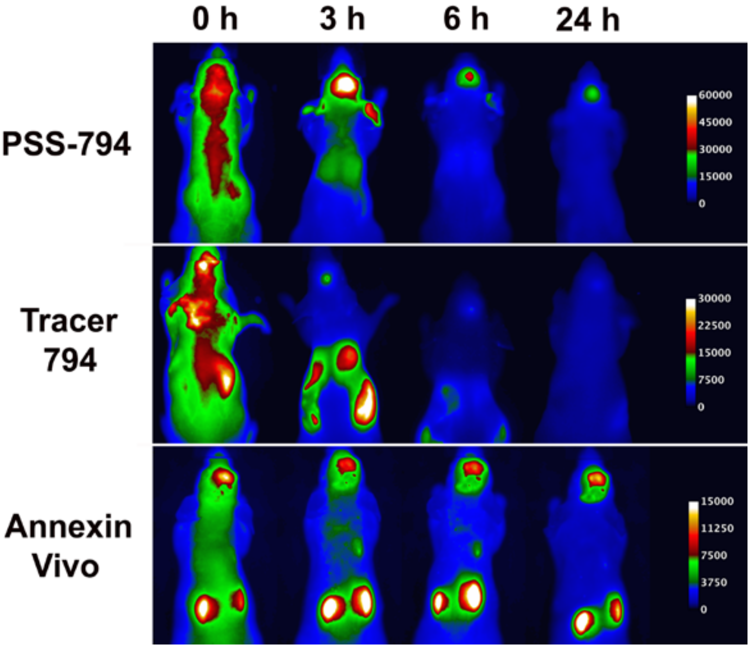

Figure 2. Representative in vivo near-infrared fluorescence montages of PSS-794, Tracer-794, and Annexin-Vivo 750 accumulation in a brain cryoinjury mouse model. A pre-cooled metal cylinder was applied to the head of each mouse for 60 s followed by intravenous injection of either PSS-794 (3.0 mg/kg), Tracer-794 (3.0 mg/kg), or Annexin-Vivo 750. Images were acquired at the indicated time points after probe injection. N = 5.

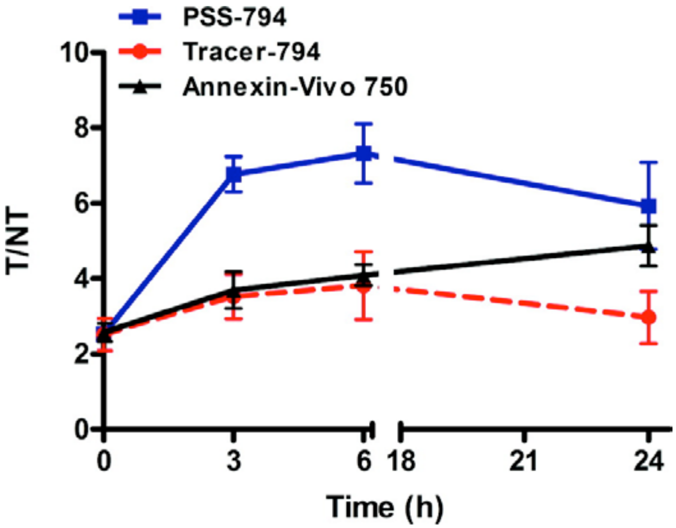

Figure 3. In vivo quantification of PSS-794, Tracer-794, and Annexin-Vivo 750 accumulating in a 60 s brain cryoinjury mouse model. Target to non-target ratios (T/NT) were calculated by region of interest (ROI) analysis of the digital images. Shapes were drawn around the site of the cryoinjury (target, T) and around an equivalent site on the lower back (non-target, NT) and the mean pixel intensities (MPI) were recorded. T/NT ±SEM. N = 5. Numerical values and statistical significance are shown in Table S1.

At 24 h after probe injection, the mice were sacrificed and subjected to *ex vivo* imaging and histological analysis. *Ex vivo* whole-body images were acquired with 1) the skin removed from the head, which exposed the tissue over the skull, and 2) both the skin and the skull removed, which exposed the brain. ROI analysis compared the cryoinjury site *in vivo* just before animal sacrifice (labeled as Normal), to the deceased animal with skin removed (labeled as No Skin), and with both the skin and skull removed (labeled as No Skull). In each case, the MPI were recorded and normalized to the *in vivo* values. The normalized MPI for PSS-794 and Annexin-Vivo 750 decreased with each layer of tissue removed from the head (Fig. S2, Table S2). This is unusual because MPI at a deep-tissue site typically increases as the intervening skin and tissue is 10 removed [31]. It appears that PSS-794 and Annexin-Vivo 750 target the cryolesion-induced cell death that is occurring on the skin, the pericranium, and on the brain. The normalized MPI for Tracer-794 images exhibited a different trend, and increased with removal of the skin followed by a decrease in MPI with removal of the skull (Fig. S2, Table S2). But the absolute MPI for the Tracer-794 images were substantially lower than the values for the PSS-794 images ($P < 0.0005$ for Normal; $P < 0.001$ for No Skin; $P < 0.03$ for No Skull), reflecting the much greater clearance of tracer dye from the cryoinjury (Fig. S3). These spatial and temporal differences in probe localization indicate that the targeted cell death probe PSS-794 and non-targeted Tracer-794 accumulate in the brain cryoinjury by different mechanisms.

H&E micrographs of sectioned cryoinjured brains from mice sacrificed at 24 h after probe injection, showed a focal region of cell death that was surrounded by healthy brain tissue (Fig. 4A). Sections of cryoinjured brains were imaged using a fluorescence scanner to determine probe distribution throughout the brain. There was high accumulation of PSS-794 at the cryolesion site, while only negligible amounts of Tracer-794 were in the cryoinjured brain (Fig. S4). To further confirm that PSS-794 was targeting sites of brain cell death, immunohistochemisty was performed on the cryoinjured brains using an antibody specific for activated caspase-3. Fluorescence microscopy showed extensive staining of activated caspase-3 around the cryolesion, and also strong near-infrared fluorescence signal from the PSS-794 (Fig. 4B). Caspase-3 and PSS-794 staining could not be visualized in healthy regions of the brain (Fig. S6). Fluorescence from Tracer-794 could not be detected in the same regions as caspase-3 in the cryoinjured brains (Fig. S5).

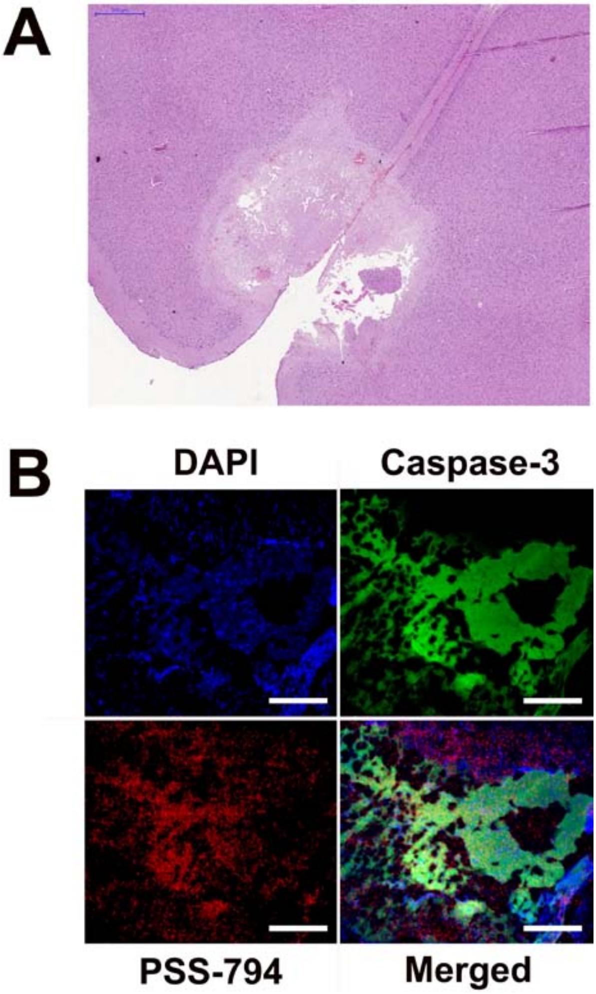

Figure 4. Representative histological micrographs from cryoinjured mouse brains. The micrographs were subjected either to H&E staining (A) or counterstained with an anti-caspase-3 antibody and DAPI (B). Images in B are from the region of the brain cryoinjury. Scale bar in A = 500 µm. Scale bar in B = 200 µm.

To determine if PSS-794 could measure TBI severity *in vivo*, the cryolesion experiment was repeated, with the time for contacting the pre-cooled metal cylinder to the mouse's head reduced to 20 s. The animals were subsequently dosed with either PSS-794 or Tracer-794 and then imaged over time (Fig. S7). As shown in Figure 5 and Table S3, T/NT values for PSS-794 and Tracer-794 were lower in the 20 s cryolesion mouse model indicating less tissue damage compared to the 60 s cryolesion. Quantification of the *ex vivo* images with skin or skull removed showed similar PSS-794 and Tracer-794 staining patterns as with the 60 s cryolesion (Fig. S2, Fig. S8).

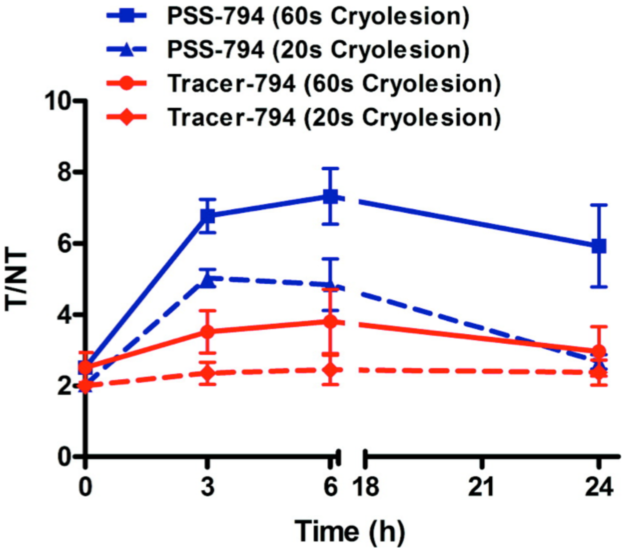

Figure 5. Comparison of PSS-794 and Tracer-794 accumulation in the 20 s and 60 s brain cryoinjury mouse models. T/NT ratios were calculated by ROI analysis. T/NT ± SEM. N = 5. Numerical values and statistical significance are shown in Table S3.

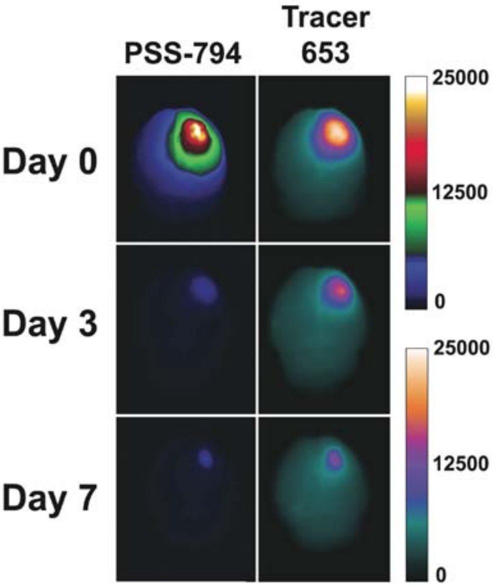

Figure 6. Multicolor fluorescence imaging of cell death and blood-brain barrier disruption in cryoinjured brains. Three cohorts of hairless mice were given a 60 s brain cryoinjury. Mice were then injected with a single dose of PSS-794 either immediately following cryoinjury (Day 0), 3 days post-cryoinjury (Day 3), or 7 days post-cryoinjury (Day 7). Each mouse was also injected with Tracer-653 at five hours post-PSS-794 injection. One hour after Tracer-653 injection, the mice were anesthetized and sacrificed. The brains were excised and placed in an epi-fluorescence imaging station for *ex vivo* imaging.

Evans Blue is routinely used to monitor BBB disruption in animal models [32,33]; thus, it served as a positive control for Tracer-653 in this mouse TBI model. Separate cohorts of cryoinjured mice were administered Evans Blue and Tracer-653. Evans Blue extravasation is typically quantified using histology; however, we utilized its weak red fluorescence emission to perform *ex vivo* imaging of the brain sections [34]. The *ex vivo* images of cryoinjured brains clearly showed accumulation of Evans Blue at Day 0 and less so at Day 3 post-injury (Fig. S12). When compared to Tracer-653, the area of Evans Blue staining was more localized at the site of cryoinjury. *In vivo*, Evans Blue binds to albumin proteins causing it to have a significantly higher molecular weight compared to Tracer-653 (67 kDa v.s. 2 kDa) [35]. The smaller effective size of Tracer-653 likely allows it to permeate into areas that are not accessible by the Evans Blue- albumin complex thus increasing the area of tissue that is stained by Tracer-653 [36,37]. Taken together, the results indicate that Tracer-653 is an effective substitute for Evans Blue as a tracer probe for monitoring BBB disruption in TBI. Compared to Evans Blue, Tracer-653 exhibits a much brighter and narrower, deep-red emission band, and thus is more amenable to multicolor optical imaging.

To determine if we could simultaneously follow cranial cell death and BBB disruption in a single animal, we injected near-infrared PSS-794 and deep-red, Tracer-653 into mice that had received cryolesions. In short, three cohorts of hairless mice were administered 60 s brain cryolesions, and then injected with PSS-794 either immediately following cryoinjury, at 3 days post-cryoinjury, or at 7 days post-cryoinjury. Each mouse was also injected with Tracer-653 at 5 h post-PSS-794 injection (the injection lag time accounts for the difference in probe clearance rates). At one hour after Tracer-653 injection, the mice were anesthetized and sacrificed. The brains were excised and placed in an epi-fluorescence imaging station for *ex vivo* imaging. As shown in Figure 6, the amount of PSS-794 accumulation in these cryoinjured brain sections decreased greatly with the age of the injury. For example, the MPI for a cryolesion section on Day 3 was six-fold lower ($P < 0.0002$) than the equivalent section on Day 0 (Fig. S10), indicating a substantial and relatively rapid decrease in the number dead and dying cells. In comparison the Tracer-653 signal in a cryoinjured brain decreased much more slowly with the age of injury. For example, the MPI for a cryolesion section on Day 7 was only about two-fold lower ($P < 0.05$) than the equivalent section on Day 0 (Fig. 6, Fig. S10). Furthermore, the amount of Tracer-653 in a cryoinjured brain on Day 7 (as judged by comparing MPI) was three times higher ($P < 0.05$) than an equivalent brain taken from a healthy control mouse treated with Tracer-653 (Fig. S11). Taken together, the Tracer-653 data consistently indicates that there is a gradual but incomplete improvement in BBB integrity over the seven-day post-cryolesion period.

Discussion

The cryoinjury TBI mouse model used in these studies is a technically simple, high- throughput version of a previously reported model that contacts a pre-cooled rod with the surgically exposed skull of mice [38,39,40]. We chose to not remove the skin around the skull because preliminary studies indicated that the cell death probes target the dead skin cells generated during the surgery, thus complicating the *in vivo* imaging. We find that the lesions caused by this adapted cryoinjury model are highly reproducible in size and location (Fig. S3) and can be clearly delineated from the rest of the brain [41]. However, this model only conditionally mimics human TBI and lacks the diffusion axonal injuries that complicate human head injuries [42]. Other TBI mouse models such as the controlled cortical impact and fluid percussion injury models can mimic the whole spectrum of focal-type brain injuries and produce axonal injuries [43]. But these models have technical drawbacks including the need for specialized equipment and the requirement to perform animal craniotomy.

We evaluated two tracers, Tracer-794 and Tracer-653, and two targeted probes, PSS-794 (2 KDa) and Annexin Vivo-750 (36 kDa), in the adapted cryolesion TBI model. The two targeted probes are functionally similar in that they identify dead and dying cells with membranes that expose phosphatidylserine; however, the probes are quite different in molecular size and blood clearance pathways. Annexin probes are known to accumulate in the kidneys, whereas, PSS-794 clears more though the liver. The *in vivo* epi-fluorescence imaging showed that the maximum T/NT ratio with PSS-794 (6.77 ± 0.47) occurred at about 3 h after probe injection and was about two times higher than the maximum T/ NT ratio with Annexin Vivo-750 (Fig. 2, Fig. 3). Both cell death probes cleared fairly slowly from the site of cryolesion. In comparison, Tracer-794 diffused in and completely out of the cryoinjury within a few hours. PSS-794 accumulation at the cryoinjury was observed to increase with injury severity, as judged by comparing the 20 s and 60 s cryolesions (Fig. 5). Thus, for pre-clinical studies that measure TBI severity in mouse models, optical imaging using PSS-794 appears to be a complementary alternate to classical methods that monitor changes in lesion volume [44].

Multicolor fluorescence imaging is a promising new method to simultaneously monitor different physiological processes [45,46], but has previously not been exploited to monitor TBI progression in mice. The highly fluorescent Tracer-653 functions like Evans Blue dye and allows optical imaging of BBB disruption. Furthermore, the deep-red emission of Tracer-653 can be distinguished from the near-infrared emission of PSS-794 in the same animal. Multicolor imaging of cryoinjured mice that were dosed with both PSS-794 and Tracer-653 enabled longitudinal tracking of the changes in cell death and BBB permeability, respectively. The PSS-794 images in Figures 6 and S10 show that the amount of cell death had decreased substantially after Day 3, presumably due to efficient dead cell clearance by animal's innate immune system [47]. But the Tracer-653 images indicate that healing and repair of the BBB was a much slower process. After Day 7, the BBB was still substantially more permeable than before the cryoinjury event, a timeframe that is consistent with previous literature observations [36,37].

In summary, we report that the synthetic near-infrared fluorescent probe, PSS-794, can be used to visualize cell death in an adapted cryolesion mouse model of TBI. The optical images with PSS-794 produced higher cryolesion signal contrast (higher T/NT ratio) than the mechanistically similar protein probe, Annexin-Vivo 750. Tracer-653 was validated as a low molecular weight, deep-red tracer dye for monitoring BBB disruption, and a binary mixture of PSS-794 and Tracer-653 was employed for multicolor imaging of cell death and BBB permeability in a single animal. The imaging data indicates that at three days after brain cryoinjury the amount of cell death had decreased significantly, but the integrity of the BBB was still impaired; at seven days the BBB was still substantially more permeable than before cryoinjury. The pathophysiological outcomes of TBI are highly heterogeneous in terms of severity and rate of progression. The time between physical trauma and the onset of secondary processes such as BBB breakdown is a potential window for therapeutic treatment [48]. It should be possible to develop this adapted cryoinjury mouse model into a high throughput, optical imaging screen of experimental therapeutics for TBI.

Methods

Ethics statement

All animal experiments were approved for animal health, ethics, and research by the Animal Welfare Committee of Leiden University Medical Center and the Institutional Animal Care and Use Committee of the University of Notre Dame. All animals received humane care and maintenance in compliance with the Code of Practice Use of Laboratory Animals in Cancer Research [49].

Probe synthesis

The synthesis and properties of Tracer-794 (λ_{ex}: 794 nm, λ_{em}: 810 nm), PSS-794 (λ_{ex}: 794 nm, λ_{em}: 810 nm) and Tracer-653 (λ_{ex}: 653 nm, λ_{em}: 673 nm) have been reported previously [50,51]. PSS-794 is commercially available as PSVue® 794 (Molecular Targeting Technologies Inc., West Chester, PA). Annexin-Vivo 750® (λ_{ex}: 755 nm, λ_{em}: 772 nm) was purchased from PerkinElmer (Waltham, MA).

Traumatic brain injury mouse models

Two cohorts of 4-6 week old athymic mice (male, ~25 g, *nu/nu*) (n = 5) were anesthetized by 2-3 % isoflurane inhalation. A metal cylinder, with a 3 mm diameter, was pre-cooled in liquid nitrogen and applied to the parietal region of each mouse's head for either 20 s or 60 s. The mice then received an intracardiac injection of either PSS-794 (3.0 mg/kg, 100 µL in 1% DMSO/H_2O) or Tracer-794 (3.0 mg/kg, 100 µL in H_2O). A cohort of athymic mice (n = 5) were subjected to a 60 s cryoinjury and received an intracardiac injection of Annexin-Vivo 750.

To investigate the progression of blood-brain-barrier disruption and cell death in traumatic brain injury, three cohorts of nude mice (male, ~25g, SKH1-E) (n=5) were anesthetized by 2-3 % isoflurane inhalation. A metal cylinder, with a 3 mm diameter, was pre-cooled in liquid nitrogen and applied to the parietal region of each mouse's head for 60 s. The mice then received a retro-orbital injection of PSS-794 (3.0 mg/kg, 100 µL in 1% DMSO/H_2O) and placed back into their cages. Five hours later, the mice received a retro-orbital injection of Tracer-653 (2.0 mg/kg, 100 µL in H_2O). One hour later, the mice were anesthetized by isoflurane inhalation and placed inside an IVIS Lumina (Caliper Life Sciences, Hopkinton, MA) configured for whole-body, epi-fluorescence imaging. After *in vivo* imaging, one cohort was sacrificed and *ex vivo* fluorescence imaging was performed on the excised brain. The other cohorts were placed back into their cages. Cohorts were subjected to the same PSS-794 and Tracer-653 injection and imaging procedures, either three or seven days post-injury (Fig. S9).

Evans Blue (Sigma, St. Louis, MO) (25 mg/kg, 100 µL in H_2O) was injected intravenously into hairless mice following 60 s brain cryolesion. The probe was allowed to circulate for one hour, then the mice were anesthetized and sacrificed. The brains were excised and placed inside an IVIS Lumina for *ex vivo* epi-fluorescence imaging. Another cohort of hairless mice was subjected to the same injection and imaging procedure three days post-injury.

In vivo near-infrared fluorescence imaging

Athymic mice were anesthetized by 2-3 % isoflurane inhalation and placed inside an IVIS Spectrum (Caliper Life Sciences, Hopkinton, MA) configured for whole-body epi-fluorescence imaging. For mice injected with PSS-794 or Tracer-794, images were acquired immediately after probe injection and at 3, 6, and 24 h time points (excitation filter: 710 nm, emission filter: 820 nm, exposure time: 1 s, bin: 8, f/stop: 2, field of view: 6.6 cm). For mice injected with Annexin-Vivo 750, images were acquired for 1 s using a 710 nm excitation filter and a 780 nm emission filter (bin: 4, f/stop: 2, field of view: 6.6 cm). After each time point, the mice were returned to their cages and fed ad libitum.

Acquired images were exported as 16 bit tiff files and region of interest (ROI) analysis was performed using ImageJ 1.44. In short, a ROI was drawn around the cryoinjury site (T) and an equal sized ROI was drawn on the lower back (NT) of each mouse (Fig. S1). The mean pixel intensity of the T and NT was measured and recorded for each mouse. The T/NT ratios were then calculated, and statistical analysis was performed to acquire the average of each ratio (n = 5) with the standard error of the mean (SEM). The resulting ROI values were plotted using Graphpad Prism 4.

Ex vivo near-infrared fluorescence imaging

Following the 24 h time point, mice were sacrificed by cervical dislocation. *Ex vivo* images were acquired with the skin from the head removed and both the skin and the skull removed to facilitate epi-fluorescence imaging with an IVIS Spectrum (excitation filter: 710 nm, emission filter: 820 nm, exposure time: 1 s, bin: 8, f/stop: 2, field of view: 6.6 cm for PSS-794 and Tracer-794) (excitation filter: 710 nm, emission filter: 780 nm, exposure time: 1 s, bin: 4, f/stop: 2, field of view: 6.6 cm for Annexin-Vivo 750).

All the nude mice were sacrificed, the brains excised and placed inside an IVIS Lumina for multicolor epi-fluorescence imaging (excitation filter: 705-780 nm, emission filter: 810-885 nm, exposure time: 5 s, bin: 2, f/stop: 2, field of view: 5 cm for PSS-794) (excitation filter: 615-665 nm, emission filter: 695-770 nm, exposure time: 8 s, bin: 2, f/stop: 2, field of view: 5 cm for Tracer-653). The ROI analysis was performed by drawing an ROI around the cryoinjury site and recording the mean pixel intensity. The resulting mean pixel intensities were plotted using Graphpad Prism 4.

Histology

Brains were flash frozen in OCT (Tissue Tek, Torrance, CA) were fixed in 4% formaldehyde, cut into 10 µm paraffin sections. Tissue sections were mounted onto slides and imaged using a LI-COR Odyssey (LI-COR Biosciences, Lincoln, NE) scanner equipped with a 785 nm diode laser. Slides were also subjected to hematoxylin and eosin (H&E) staining to determine the extent of cell death and cellular morphological changes in the cerebral cortex. Selected brain sections were incubated overnight with a rabbit anti-human polyclonal caspase-3 antibody (Abcam Inc.; 1:50). The sections were then incubated with goat anti-rabbit IgG conjugated to Alexa-Fluor 488 (Invitrogen; 1:500) for 15 min, and counterstained with DAPI. Fluorescence images of the sections were acquired using a Nikon TE-2000 U epi-fluorescence microscope equipped with the appropriate UV (ex. 340/80 nm, em. 435/85 nm), GFP (ex. 450/90 nm, em. 500/50 nm), and near-infrared filters (ex. 710/75 nm, em. 810/90 nm). Fluorescence images were captured using Metamorph software (Universal) and analyzed using ImageJ 1.44.

Statistical analysis

Results are depicted as mean ± standard error of the mean (SEM). Statistical analysis was performed using a Student’s t-test.

Acknowledgements

We thank the Notre Dame Histology Core and the Notre Dame Integrated Imaging Facility for preparation of histological sections and access to whole animal imaging equipment. This study was supported by the Center for Translational Molecular Medicine, project MUSIS (grant 03O-202); NIH grants R01GM059078 (B.D.S.) and T32GM075762 (B.A.S.), Volkswagen grant I83443, and the ENCITE project 201842.

Supporting Information:

Additional imaging data and quantitative analysis are available free of charge via the Internet at http://pubs.acs.org.

References

1. Faul, M., Xu, L., Wald, M. M. & Coronado, V. G. Traumatic Brain Injury in the United States: Emergency Department Visits, Hospitalizations, and Deaths, 2002-2006. *National Center for Injury Prevention and Control, Centers for Disease Control and Prevention*, 1-71 (2010).
2. Thurman, D. J., *et al.* Traumatic Brain Injury in the United States: a Public Health Perspective. *J. Head Trauma Rehabil.* **14**, 602-615 (1999).
3. Werner, C. & Engelhard, K. Pathophysiology of Traumatic Brain Injury. *Br. J. Anaesth.* **99**, 4-9 (2007).
4. Kim, J. J. & Gean, A. D. Imaging for the Diagnosis and Management of Traumatic Brain Injury. *Neurotherapeutics* **8**, 39-53 (2011).
5. Wilson, J. R. F. & Green, A. Acute Traumatic Brain Injury: a Review of Recent Advances in Imaging and Management. *Eur. J. Trauma Emerg. Surg.* **35**, 176-185 (2009).
6. Chapon, C., *et al.* Imaging E-Selectin Expression Following Traumatic Brain Injury in the Rat using a Targeted USPIO Contrast Agent. *Magn. Reson. Mater. Phy.* **22**, 167-174 (2009).
7. Reshef, A., *et al.* Targeting Cell Death In Vivo in Experimental Traumatic Brain Injury by a Novel Molecular Probe. *J. Neurotrauma* **25**, 569-580 (2008).
8. Kosaka, N., *et al.* In Vivo Real-Time, Multicolor, Quantum Dot Lymphatic Imaging. *J. Invest. Dermatol.* **129**, 2818-2822 (2009).
9. Yamamoto, N., Tsuchiya, H. & Hoffman, R. M. Tumor Imaging with Multicolor Fluorescent Protein Expression. *Int. J. Clin. Oncol.* **16**, 84-91 (2011).
10. Mitsunaga, M., *et al.* In Vivo Longitudinal Imaging of Experimental Human Papillomavirus Infection in Mice with a Multicolor Fluorescence Mini-Endoscopy System. *Cancer Prev. Res.* **4**, 767-773 (2011).
11. Blankenberg, F. G. In Vivo Detection of Apoptosis. *J. Nucl. Med.* **49**, 81S-95S (2008).
12. Zhao, M. In Vivo Apoptosis Imaging Agents and Strategies. *Anti-Cancer Agents Med. Chem.* **9**, 1018- 1023 (2009).
13. Niu, G., & Chen, X. Apoptosis Imaging: Beyond Annexin V. *J. Nucl. Med.* **51**, 1659-1662 (2010).
14. Ntziachristos, V., *et al.* Visualization of Antitumor Treatment by Means of Fluorescence Molecular Tomography with an Annexin V-Cy5.5 Conjugate. *Proc. Natl. Acad. Sci. U.S.A.* **101**, 12294-12299 (2004).
15. Beekman, C. A., *et al.* Questioning the Value of (99m)Tc-HYNIC-Annexin V Based Response Monitoring after Docetaxel Treatment in a Mouse Model for Hereditary Breast Cancer. *Appl. Radiat. Isot.* **69**, 656-662 (2011).
16. Vanderheyden, J. L., *et al.* Evaluation of 99mTc- MAG3-Annexin V: Influence of the Chelate on In Vitro and In Vivo Properties in Mice. *Nuc. Med. Biol.* **33**, 135- 144 (2006).
17. Lederle, W., *et al.* Failure of Annexin-Based Apoptosis Imaging in the Assessment of Antiangiogenic Therapy Effects. *EJNMMI Research* **1**, 26 (2011).
18. Burtea, C., *et al.* Peptidic Targeting of Phosphatidylserine for the MRI Detection of Apoptosis in Atherosclerotic Plaques. *Mol. Pharmaceutics* **6**, 1903-1919 (2009).
19. Zheng, H., Wang, F., Wang, Q. & Gao, J. Cofactor-Free Detection of Phosphatidylserine with Cyclic Peptides Mimicking Lactadherin. *J. Am. Chem. Soc.* **131**, 15280-15283 (2011).
20. Xiong, C., *et al.* Peptide-Based Imaging Agents Targeting Phosphatidylserine for the Detection of Apoptosis. *J. Med. Chem.* **54**, 1825-1835 (2011).
21. Hanshaw, R.G. & Smith, B.D. New Reagents for Phosphatidylserine Recognition and Detection of Apoptosis. Bioorg. *Med. Chem.* **13**, 5035-5042 (2005).
22. Smith, B.A., *et al.* Optical Imaging of Mammary and Prostate Tumors in Living Animals using a Synthetic Near Infrared Zinc(II)-Dipicolylamine Probe for Anionic Cell Surfaces. *J. Am. Chem. Soc.* **132**, 67-69 (2010).
23. Smith, B.A., *et al.* In Vivo Optical Imaging of Acute Cell Death using a Near-Infrared Fluorescent Zinc-Dipicolylamine Probe. *Mol. Pharmaceutics* **8**, 583-590 (2011).
24. Smith, B. A., *et al.* In Vivo Targeting of Cell Death using a Synthetic Fluorescent Molecular Probe. *Apoptosis* **16**, 722-731 (2011).

25. Bahamni, P., *et al.* Visualization of Cell Death in Mice with Focal Cerebral Ischemia using Fluorescent Annexin A5, Propidium Iodide, and TUNEL Staining. *J. Cereb. Blood Flow Metab.* **31**, 1311-1320 (2011).
26. O'Neil, E. J., & Smith, B. D. Anion Recognition using Dimetallic Coordination Complexes. *Coord. Chem. Rev.* **250**, 3068-3080 (2004).
27. Abulrob, A., Brunette, E., Slin, J., Baumann, E., & Stanimirovic, D. Dynamic Analysis of the Blood- Brain Barrier Disruption in Experimental Stroke using Time Domain In Vivo Fluorescence Imaging. *Mol. Imaging* **7**, 248-262 (2008).
28. Hawkins, B. T., & Egleton, R. D. Fluorescence Imaging of Blood-Brain Barrier Disruption. *J. Neurosci. Meth.* **151**, 262-267 (2006).
29. Murakami, K., *et al.* Cold Injury in Mice: a Model to Study Mechanisms of Brain Edema and Neuronal Apoptosis. *Prog. Neurobiol.* **57**, 289-299 (1999).
30. Lin, K. J., *et al.* In Vivo Imaging of Radiation-Induced Tissue Apoptosis by 99mTc(I)-his6-Annexin A5. *Ann. Nucl. Med.* DOI: 10.1007/s12149-012-0571-x (2012).
31. Leblond, F., Davis, S.C., Valdés, P.A., & Pogue, B. W. Pre-Clinical Whole-Body Fluorescence Imaging: Review of Instruments, Methods and Applications. J. Photochem. *Phototbiol.* **B 98**, 77-94 (2010).
32. Belayev, L., Busto, R., Zhao, W., & Ginsberg, M. D. Quantitative Evaluation of Blood-Brain Barrier Permeability Following Middle Cerebral Artery Occlusion in Rats. *Brain Res.* **739**, 88-96 (1996).
33. Del Valle, J., Camins, A., Pallás, M., Vilaplana, J., & Pelegri, C. A New Method for Determining Blood-Brain Barrier Integrity Based on Intracardiac Perfusion of an Evans Blue-Hoechst Cocktail. *J. Neurosci. Meth.* **174**, 42-49 (2008).
34. Saria, A., & Lundberg, J. M. Evans Blue Fluorescence: Quantitative and Morphological Evaluation of Vascular Permeability in Animal Tissues. *J. Neurosci. Meth.* **8**, 41-49 (1983).
35. Wolman, M. *et al.* Evaluation of the Dye-Protein Tracers in Pathophysiology of the Blood-Brain Barrier. *Acta Neuropathol.* **54**, 55-61 (1981).
36. Habgood, M. D., *et al.* Changes in Blood-Brain Barrier Permeability to Large and Small Molecules Following Traumatic Brain Injury in Mice. *Eur. J. Neurosci.* **25**, 231-238 (2007).
37. Lotocki, G., *et al.* Alterations in Blood-Brain Barrier Permeability to Large and Small Molecules and Leukocyte Accumulation after Traumatic Brain Injury: Effects of Post-Traumatic Hypothermia. *J. Neurotrauma* **26**, 1123-1134 (2009).
38. Raslan, F., *et al.* Inhibition of Bradykinin Receptor B1 Protects Mice from Focal Brain Injury by Reducing Blood-Brain Barrier Leakage and Inflammation. *J. Cereb. Blood Flow Metab.* **30**, 1477-1486 (2010).
39. Stoffel, M., *et al.* Identification of Brain Tissue Necrosis by MRI: Validation by Histomorphometry. *J. Neurotrauma* **21**, 733-740 (2004).
40. Spaeth, N., *et al.* Uptake of 18F-Fluorocholine, 18F-Fluoroethyl-L-Tyrosine, and 18F-FDG in Acute Cerebral Radiation Injury in the Rat: Implications for Separation of Radiation Necrosis from Tumor Recurrence. *J. Nucl. Med.* **45**, 1931-1938 (2004).
41. Albert-Weissenberger, C. & Sirén, A. L. Experimental Traumatic Brain Injury. *Exp. Trans. Stroke Med.* **2**, 16-23 (2010).
42. Gaetz, M. The Neurophysiology of Brain Injury. *Clin. Neurophysiol.* **115**, 4-18 (2004).
43. O'Connor, W. T., Smyth, A. & Gilchrist, M. D. Animal Models of Traumatic Brain Injury: a Critical Evaluation. Pharmacol. *Therapeut.* **130**, 106-113 (2011).
44. Eriskat, J., Fürst, M., Stoffel, M. & Baethmann, A. Correlation of Lesion Volume and Brain Swelling from a Focal Brain Trauma. *Acta Neurochir.* **86**, 265-266 (2003).
45. Kobayashi, H., *et al.* Simultaneous Multicolor Imaging of Five Different Lymphatic Basins using Quantum Dots. *Nano Lett.* **7**, 1711- 1716 (2007).
46. Yang, M., Jiang, P. & Hoffman, R. M. Whole-Body Subcellular Multicolor Imaging of Tumor-Host Interaction and Drug Response in Real Time. *Cancer Res.* **67**, 5195-5200 (2007).
47. Giulian, D., *et al.* The Role of Mononuclear

Phagocytes in Wound Healing After Traumatic Injury to Adult Mammalian Brain. *J. Neurosci.* **9**, 4416-4429 (1989).

48. Shloesberg, D., Benifa, M., Kaufer, D. & Friedman, A. Blood-Brain Barrier Breakdown as a Therapeutic Target in Traumatic Brain Injury. *Nat. Rev. Neurol.* **6**, 393-403 (2010).
49. Netherlands Inspectorate for Health Protection, Commodities and Veterinary Public Health Code of Practice Animal Experiments in Cancer Research. Inspectie W&V, 1-22 (1999).
50. Leevy, W. M., *et al.* Optical Imaging of Bacterial Infection in Living Mice using a Near-Infrared Molecular Probe. *J. Am. Chem. Soc.* **128**, 16476-16477 (2006).
51. Cole, E. L., *et al.* Water-Soluble, Deep-Red Fluorescent Squaraine Rotaxanes. Org. Biomol. Chem. DOI: 10/1039/c2ob06783h (2011).